Article

Electronic Structure of Orthorhombic $Bi_4V_2O_{11}$ and Role of Gap States in Photoelectrochemical Water Splitting

Jiaqi Liu, Kenichi Ozawa, Namiki Uezono, Sachin A. Pawar, Shugo Suzuki, Aboulaye Traoré, Muhammad Monirul Islam, Kazuhiko Mase, and Takeaki Sakurai*

Cite This: https://doi.org/10.1021/acs.jpcc.3c01238

Read Online

ACCESS | 📊 Metrics & More | 📖 Article Recommendations | SI Supporting Information

ABSTRACT: A group of bismuth vanadium oxides shows promise as an excellent material for photoanodes in water splitting. However, the efficiency of $Bi_4V_2O_{11}$ in water splitting is not satisfactory compared to $BiVO_4$. In this study, we investigated the electronic structure of orthorhombic $Bi_4V_2O_{11}$ using density functional theory (DFT) and synchrotron soft X-ray spectroscopy techniques to clarify the causes of inefficiency. Our DFT calculations of the two-fold superlattice, as confirmed by near-edge X-ray absorption fine structure measurements, revealed its indirect-band-gap nature. An angle-resolved photoelectron spectroscopy study identified the states within the band gap, and the resonant photoemission technique and DFT simulation clarified that the origin of the gap states was anisotropic localization of electrons around V−O tetrahedra. Water absorption enhances the gap states, which dramatically impedes the kinetics of water oxidation reactions. Our results reveal the role of gap states in water oxidation reactions and offer new insights into manipulating gap states in 3d transition metal oxides.
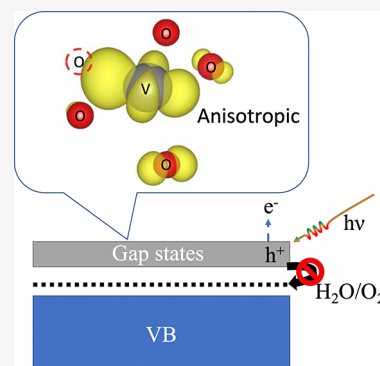
INTRODUCTION

The development of n-type semiconductors has been actively promoted as a photoanode for efficient conversion of solar energy into chemical fuel (hydrogen) via photoelectrochemical water splitting. The materials with narrower band gaps have been paid more attention to eliminate the band gap's limitation on solar-to-hydrogen efficiency and realize practical applications. $Bi_4V_2O_{11}$, a typical Bi-rich phase depicted in the phase diagram of Bi_2O_3-V_2O_5,[1−3] has been used in photocatalysis for degrading organic compounds.[4,5] Among the various polymorphs of $Bi_4V_2O_{11}$, the low-temperature stable phases (i.e., monoclinic and orthorhombic $Bi_4V_2O_{11}$)[6,7] have received more attention in the field of photocatalysis. The oxidation reaction of water by orthorhombic $Bi_4V_2O_{11}$ was first reported in 2016,[8] expanding its potential application as a new solar water oxidation photocatalyst. However, the photocatalytic performance of water splitting in $Bi_4V_2O_{11}$ is unsatisfactory. Even after minimizing the effects of crystal defects using epitaxial techniques, the orthorhombic $Bi_4V_2O_{11}$ showed a very low photocurrent in the water oxidation reaction.[9] The behavior of electrons and holes is crucial in the photocatalysis process. Hence, the electronic structure needs to be investigated to understand carrier properties and explore the reasons for inefficiency in water splitting.

In previous studies, the electronic structure of the orthorhombic $Bi_4V_2O_{11}$ material has been investigated using density functional theory (DFT) calculations. According to these studies, orthorhombic $Bi_4V_2O_{11}$ is a direct band gap material with a valence band maximum (VBM) and a conduction band minimum (CBM) located at the Gamma points of the bulk Brillouin zone.[8,10] However, the structure complexity of the oxygen atoms in the material, as reported in an experimental study,[6,11] has made it challenging to choose the appropriate unit cell for DFT calculations. An early study proposed that the structure of orthorhombic $Bi_4V_2O_{11}$ can be described using corner-sharing BiO_4 tetrahedra and distorted corner-sharing VO_6 octahedra (Aba2, a = 5.598(2) Å, b = 15.292(9) Å, c = 5.532(2) Å).[12] So far, the DFT study of orthorhombic $Bi_4V_2O_{11}$ has been based on the VO_6 octahedral structure.[8] Later research suggests that the two-fold super-lattice characteristic (Amam, a = 11.2333(2) Å, b = 5.64925(7) Å, c = 15.3471(2) Å) of the orthorhombic structure is the result of an ordering process involving corner-sharing V−O tetrahedra and disordered trigonal bipyramids.[6] However, due to the alternative unit cells, further identification of the local V−O construction is necessary to validate our understanding of the electronic structure of orthorhombic $Bi_4V_2O_{11}$. Currently, experimental work on the electronic structure of orthorhombic $Bi_4V_2O_{11}$ is still insufficient to explain the reason for its inefficiency.
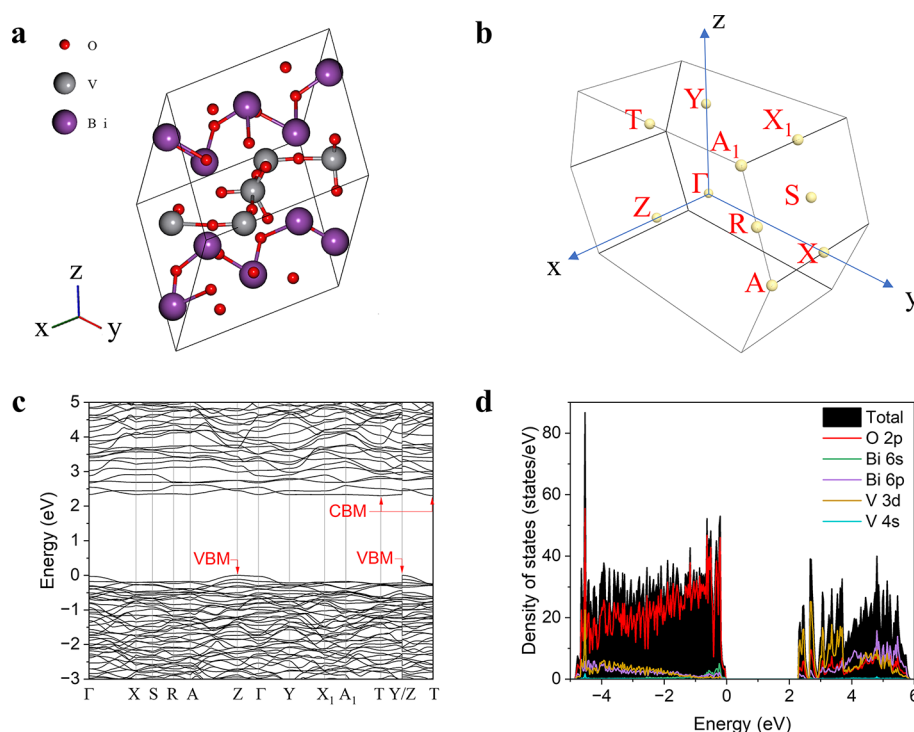
Figure 1. (a) Optimized primitive cell (base-centered) of orthorhombic $Bi_4V_2O_{11}$. (b) Brillouin zone of orthorhombic $Bi_4V_2O_{11}$ with the coordinates in real space. (c) Electronic band structure of $Bi_4V_2O_{11}$. The Bravais lattice is base-centered orthorhombic. (d) DOS and pDOS of orthorhombic $Bi_4V_2O_{11}$ onto orthogonalized atomic wavefunctions. The VBM is aligned with zero energy.

In recent studies, it has been discovered that doped $BiVO_4$ exhibits gap states in its electronic structure caused by polaron states resulting from the coupling between the hole and lattice degree of freedom.[13,14] Although the existence of gap states in $BiVO_4$ has been mostly related to the V^{4+} produced via doping, understanding the precise nature of gap states is important for manipulating the photoelectric properties of these materials. The unoccupied V 3d orbitals and charge inhomogeneities lead to an anisotropic small-hole polaron state in epitaxial $BiVO_4$,[15] shedding light on the role of electron occupations in gap states. Therefore, investigating the occupied gap states is necessary. Similar gap states were also found in $Bi_4V_2O_{11}$, which offers better conductivity of epitaxial substrates for photoelectronic characterizations compared to the insulating yttrium-doped zirconium oxide substrate of epitaxial $BiVO_4$. These gap states have been identified as a critical factor in suppressing the photoelectrochemical performance by affecting the recombination of charge carriers and charge mobility at the surface. Understanding the electronic structure $Bi_4V_2O_{11}$ can provide insights into the role of gap states in photocatalytic water splitting and is also valuable in manipulating the gap states in 3d transition metal oxides.

■ EXPERIMENTAL METHODS

Epitaxial $Bi_4V_2O_{11}$ Films. Epitaxial orthorhombic $Bi_4V_2O_{11}$ films were fabricated on a Nb-doped $SrTiO_3$ (001) substrate (Nb: 0.05 wt %, SHINKOSHA CO., LTD.) by sputtering a BiV_2O_x target (Φ60 mm, Bi_2O_3 + $2V_2O_5$). The lattice parameter of cubic $SrTiO_3$ is a = 3.905 Å, allowing the epitaxial $Bi_4V_2O_{11}$ films to align on the $SrTiO_3$ substrate with a 45° rotation, despite the lattice mismatch of approximately 2%. The sputtering process was adjusted to maintain the film composition, and thin films (~50 nm) were prepared using 120 W RF-power in an oxygen partial pressure of 5% (O_2: Ar = 5: 95) with a fixed total pressure of 0.7 Pa for 10 min, at a substrate temperature of 400 °C. The X-ray diffraction pattern of the prepared film is shown in Figure S1.

DFT Calculations. The DFT calculations were performed using the Quantum Espresso package[16−18] with pseudopotentials obtained from the standard solid-state pseudopotential precision library.[19] Kinetic energy cutoffs of 100 and 900 Ry for wave functions and charge density, respectively, were set for all calculations using the Perdew−Burke−Ernzerhof functional. The initial crystal structure of the orthorhombic $Bi_4V_2O_{11}$ was based on a previous study.[6] The optimized base-centered primitive cell of a two-fold superlattice (a = 5.8165 Å, b = 15.3799 Å, c = 11.2523 Å) was used for calculations with a $4 \times 4 \times 2$ k-point grid and tetrahedral occupations. Self-consistent field methods included spin-orbit coupling. The oxygen-deficient lattice was created by removing one oxygen atom from the V−O tetrahedra of the pristine lattice. BURAI and Vesta software[20] were used for visualization and manipulation of input files.

Experimental Characterizations. The angle-resolved photoemission spectroscopy (ARPES) measurements were performed at the Photon Factory's beamline 3B, which is part of the High Energy Accelerator Research Organization (KEK-PF) located in Tsukuba, Japan.[21] The films were heated to 500 °C for 60 min in an ultrahigh vacuum (~10^{-10} Torr) and then cooled to room temperature. Subsequently, the samples were heated to 500 °C in 6×10^{-6} Torr of O_2 (g) and cooled to room temperature. The valence band (VB) spectra were monitored in situ to minimize impurity signals. The photoelectrons were detected at an angle resolution of 1°, using an electronic energy analyzer (VSW HA54). The energy resolution was 50 meV, using a pass energy of 10 eV. The Fermi level was determined by the Fermi edge of Ta metal,

which was in contact with the films. The water adsorption experiment was also done at beamline 3B. The sample was transferred to the preparation chamber, the vapor of ultrapure water (Kanto Chemical Co., Inc.) was introduced to this chamber, and the pressure was kept at 5×10^{-6} Torr for 60 min. After adsorption, the sample was transferred back to the analysis chamber for measuring the VB spectra in an ultrahigh vacuum. The work function was determined by measuring the secondary electron cutoff and the Fermi level.

X-ray photoelectron spectroscopy (XPS) and near-edge X-ray absorption fine structure (NEXAFS) measurements were performed at beamline 13B of KEK-PF.[22,23] A hemispherical electron energy analyzer (Gammadata-Scienta SES200) was used to acquire photoelectron spectra with a typical energy resolution of 0.13 eV at a photon energy of 700 eV.[23,24] Core-level XPS spectra were measured at a photon energy of 700 eV and normalized using the photon flux recorded by monitoring the photocurrent of the final stage mirror. Binding energies were referenced to the Au $4f_{7/2}$ peak at 84.0 eV.[25] The base pressure in the analysis chamber was approximately 4.0×10^{-10} Torr. The resonant XPS measurements were conducted by acquiring VB spectra using photon energies where intensive absorption occurs across the V L_3 edges. For the NEXAFS measurements, both horizontal and vertical X-ray polarizations were used. The incidence angle of the light was 65° (relative to the normal surface direction), and the total electron yield[26] was collected by measuring the sample current. The photon energy varied from 510 to 550 eV with a step of 0.1 eV, involving the V $L_{3,2}$ edges and O K edges. The exit-slit width was 30 μm. All ARPES, XPS, and NEXAFS measurements were conducted at room temperature unless otherwise specified.

■ RESULTS AND DISCUSSION

Based on the space group of orthorhombic $Bi_4V_2O_{11}$, the base-centered orthorhombic was chosen as the Bravais lattice (as shown in Figure 1a,b). The calculated band structure based on the two-fold superlattice is presented in Figure 1c with all the high-symmetric points in the first Brillouin zone (BZ).[27] The results indicate that the VBM is located at the Z point, and the CBM is at the T point, suggesting that orthorhombic $Bi_4V_2O_{11}$ is an indirect-band gap semiconductor, with a band gap of 2.31 eV, which is consistent with previous experimental results.[8] It should be noted that the energy difference in VB top between the Γ point and VBM is only 26 meV, which is comparable to the level of thermal excitation energy at room temperature. Similarly, the energy difference in the conduction band (CB) bottom between the Γ point and CBM is 33 meV. Therefore, the indirect nature of the band gap is not significant at room temperature. However, the weak photoluminescence emission typically observed in $Bi_4V_2O_{11}$ is a characteristic of the indirect band gap nature.[2] It is worth noting that this result is not far from the previously reported DFT result,[10] despite the slight change in the unit cell.

To understand the contribution of atomic orbitals to the VB and CB, the density of states (DOS) and projected density of states (pDOS) were computed and are presented in Figure 1d. The VB and CB are mainly composed of O 2p, V 3d, V 4s, Bi 6s, and Bi 6p orbitals, which is similar to the electronic structure of $BiVO_4$.[28] The VB is primarily composed of O 2p orbitals, including the π bonding with Bi 6p, σ and π bonding with V 3d in the low-energy region, and σ bonding with Bi 6s in the top VB region.[29] The low-energy CB region is mainly

composed of V 3d orbitals with hybridization of O 2p, forming the π* antibonding. Therefore, under visible light, the electron transition typically occurs from the occupied hybridization states of Bi 6s−O 2p to the unoccupied hybridization states of V 3d−O 2p.

Low energy electron diffraction (LEED) was used to characterize the $Bi_4V_2O_{11}$ surface after the cleaning process described in the Experimental Methods Section (Supplementary Information). The LEED results show that the crystal surface presents a $\frac{\sqrt{2}}{4} \times \frac{\sqrt{2}}{2} R45°$. Rectangular LEED patterns result from the surface reconstruction of the (001) surface (Figure S2). First, the photon-energy-dependent ARPES measurements were carried out to find photon energy that captures a high-symmetry Γ point (Figure S3). The photon energy of around 59 eV corresponds to the Γ point of 5th BZ in the k_z direction (Figure 2a); then, the dispersion in the $k_x − k_y$ plane was measured using this photon energy.

Figure 2a displays the BZ of the base-centered orthorhombic $Bi_4V_2O_{11}$, taking into account the surface reconstruction. According to the characteristic of ARPES,[30] the momentum space in the surface BZ can be detected, corresponding to a projection of the bulk BZ. The projected surface BZ has a similar rectangular shape to the LEED pattern obtained (Figure S2). In Figure 2b, energy distribution curves (EDCs) along the selected high-symmetry direction (k_x) of the surface BZ were measured using a photon energy of 59 eV. The EDCs show a broad emission between the binding energy (BE) of 9 and 2 eV. Compared to DFT results (Figure 1b), the peak at 4.2 eV can be assigned to the O 2p state. The 6.5 and 8.0 eV states are attributed to mixed hybridization states of V 3d−O 2p and Bi 6p−O 2p. The top VB band (BE around 3 eV) of $Bi_4V_2O_{11}$ is mainly composed of a O 2p state and a small contribution of the Bi 6s state. Some emission peaks (such as ∼3 eV) show substantial energy shifts depending on the emission angle of the analyzer, reflecting energy dispersion of the valence states along the high-symmetry direction of the BZ. It is worth noting that the sample has a slight charge effect due to resistivity, leading to the overvalued (∼0.5 eV) BE at room temperature (Figure S4).

To clarify the energy dispersion of the VB clearly, band maps are constructed by plotting the second derivatives of the measured EDCs. The ARPES maps give the symmetric band structure and distinct dispersion concerning the $\bar{\Gamma}$ point (Figure 2c). The ARPES results of the in-plane wavevectors (k_x) show the clear dispersion of the top VB (∼3 eV). The dispersion was also found in other in-plane k paths (k_y) (Figure S5). However, this dispersion state is not the VBM band. In the calculated k-resolved DOS (Figure S6), the top band's energy level is lower than 0 (VBM). Analogously, the experimental band structure of Mo-$BiVO_4$ shows tiny dispersion in the top VB.[13] The top VB of both $BiVO_4$ and $Bi_4V_2O_{11}$ are composed of a hybrid state between the Bi 6s states and O 2p states.[31] Therefore, it is imperfect to correlate the band at 3 eV with the mobility property. Notably, the calculated band structure is consistent with the experimental ARPES results, suggesting the validity of DFT calculations in exploring the electronic structure.

Figure 2b,c shows a state in the band gap region above the VB with a BE of 1.6 eV. The lack of dispersion of this gap state suggests strong localization in real space, which is attributed to the formation of polaron states.[13] Notably, similar gap states exist in α-Fe_2O_3,[32] which can limit carrier transport. XPS was
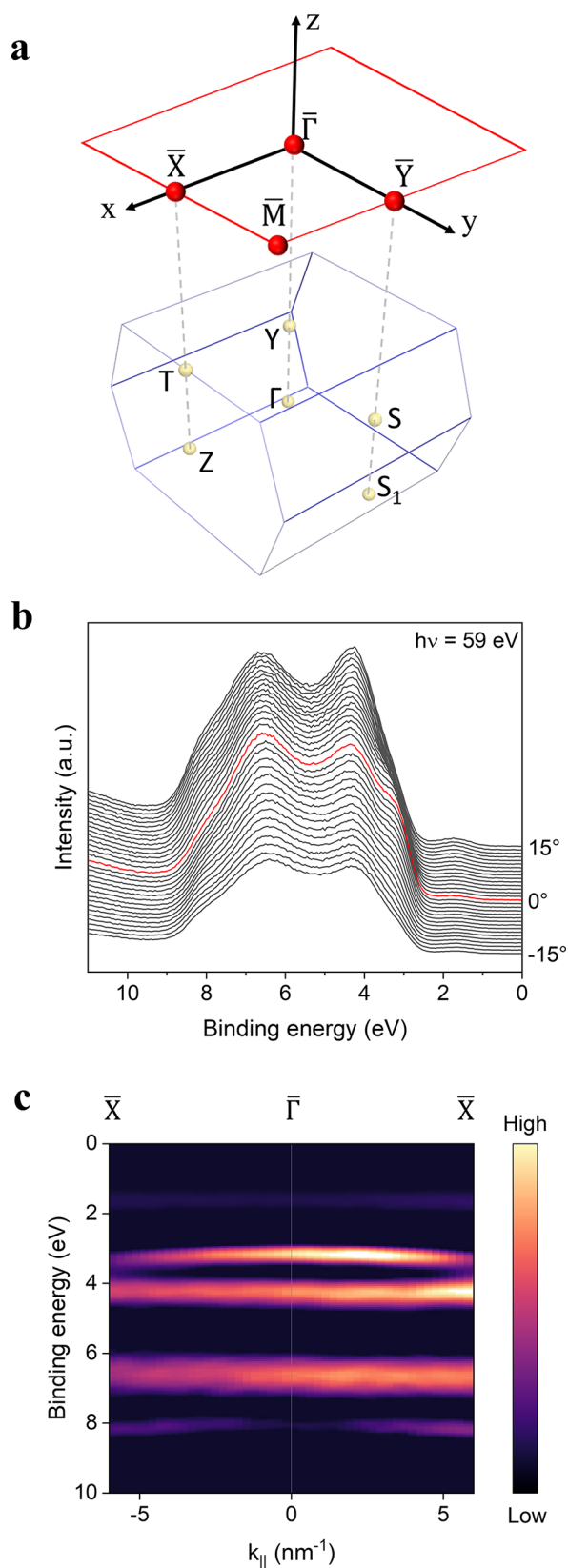
Figure 2. (a) Bulk Brillouin zone (blue lines) and the corresponding (001) surface Brillouin zone (red lines). (b) EDCs in the VB region, with the angle of the analyzer from −15 to 15°. EDC at the $\bar{\Gamma}$ point is indicated by a red line. (c) ARPES second derivatives plot along the $\bar{\Gamma}$−$\bar{X}$ direction, derived from EDCs.

used to analyze the oxidation states of Bi, V, and O on the $Bi_4V_2O_{11}$ (001) surface to determine their relation to the gap states. Survey spectra were collected to understand the elemental composition on the surface (Figure S7). All the characteristic emissions of Bi, V, and O were observed, except for a small amount of carbon. Figure 3a−d shows the XPS spectra of core levels and VB. The BE of the Bi $4f_{7/2}$ (159.6 eV) and O 1s core levels (530.4 eV) are consistent with the Bi^{3+} and O^{2-} BE but slightly higher than that observed in $Bi_4V_2O_{11}$ films[9] due to a slight charge effect. The $2p_{3/2}$ peak of V is centered at a BE of 517.2 eV, aligning with the V^{5+} oxidation state.[33] However, the V peaks have shoulder peaks at lower BEs (Figure 3b), suggesting a low valence state of V. The low oxidation states of vanadium concerning gap states have been observed in $BiVO_4$, indicating local lattice distortions of VO_4 tetrahedral symmetry.[15] Additionally, the O 1s core level spectrum is not symmetric (Figure 3a) due to a weak shoulder peak at around 532 eV, attributed to metal hydroxyls or oxygen vacancies. Importantly, the gap states (∼1.6 eV) were observed in the band gap region (Figure 3d), which is not consistent with the calculated band structure above. This implies that some structural changes occur compared to the ideal crystal structure. The V−O surroundings were assumed to be responsible for forming gap states according to the change in the chemical states of V and O atoms. Experimentally, we detected a decrease in gap states by annealing the films in an oxygen environment (6.0×10^{-6} Torr) (Figure S8). Therefore, it is inferred that the oxygen vacancies or surficial adsorption may be responsible for the gap states.

To investigate the local structure, we performed NEXAFS measurements using total electron yield[26] detection at the V $L_{3,2}$ edges. Because of the narrow bandwidth of the 3d valence electron state and the large valence-electron core-hole interaction, it can be considered that the excitons generated in the X-ray absorption process have strong localization.[34] The NEXAFS spectra involve the electronic transitions: V $2p_{3/2,1/2}$ → V 3d (Figure 3e). The intensive absorption at 516.5 and 518.6 eV for the V L_3 edge is attributed to the analogous tetrahedral crystal field (e-t_2). Other peaks at 515.7 and 517.7 eV are attributed to atomic multiplet effects or the distorted tetrahedra.[35] The crystal field splitting determined for $Bi_4V_2O_{11}$ is 2.1 eV, similar to the reported 2.2 eV of Mo (1 at.%): $BiVO_4$ (010),[14] suggesting an analogous local environment (V−O tetrahedra) of V atoms in these two materials. In contrast, the crystal field splitting of VO_6 octahedra has been reported as 2.9 eV in V_2O_5.[14] These results suggest that the orthorhombic $Bi_4V_2O_{11}$ should have a two-fold superlattice characterizing structure involving corner-sharing V−O tetrahedra, rather than corner-sharing VO_6 octahedra. Therefore, the DFT calculation in this work was based on this structure.

Based on the NEXAFS results, resonant XPS was employed to understand the composition of the VB. Two photon energies, which were resonantly absorbed, were chosen to measure XPS and compared with off-resonant XPS (Figure 3f). Intensive enhancements in the VB spectra were observed at a BE of 6.5 eV, which was attributed to V−O σ bonding,[28] consistent with the pDOS results mentioned earlier. Moreover, the gap states exhibited resonant enhancement. Resonant XPS was also checked for Bi and O elements, and the results showed no specific enhancement in the gap states concerning Bi-res (Bi-resonant, 445.3 eV, 4d → 6p) and O-res (O-resonant, 532 eV, 1s → 2p) photon-energies (Figure S9). It was inferred that the gap states originated from the V 3d
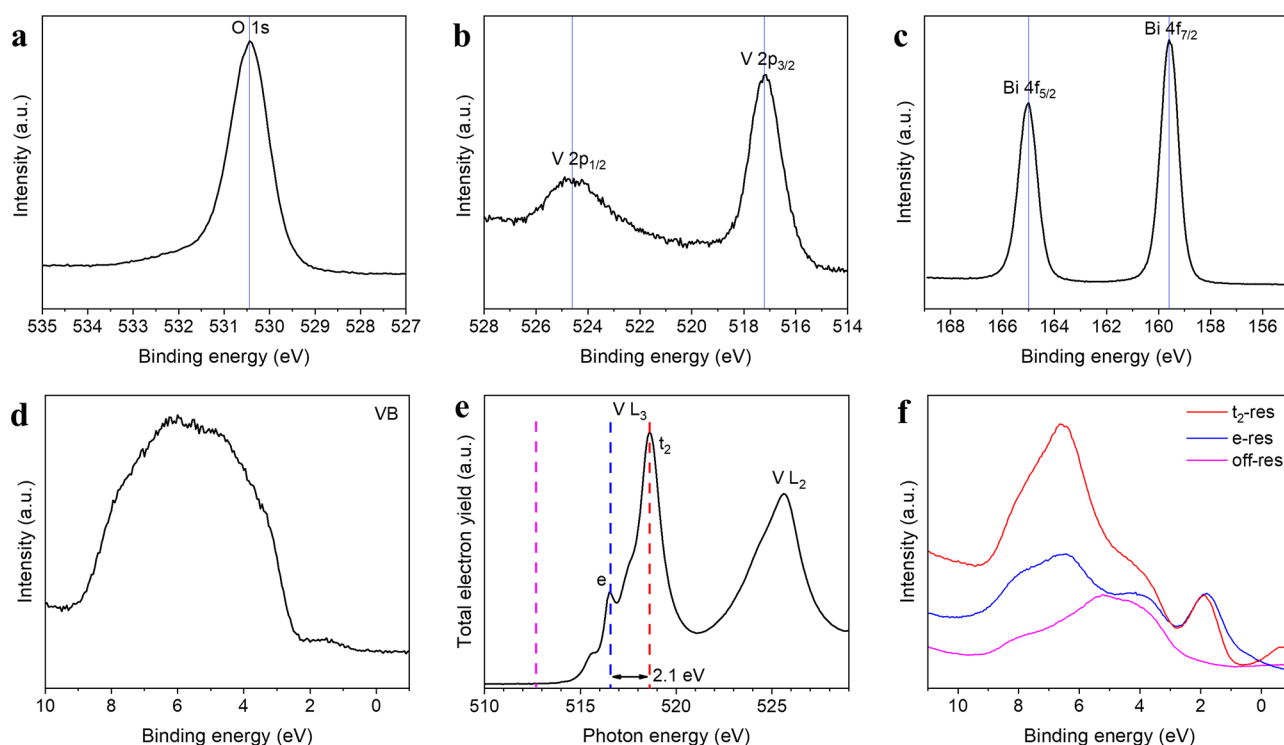
Figure 3. XPS spectra of the $Bi_4V_2O_{11}$ (001) surface: (a) O 1s, (b) V 2p, (c) Bi 4f, and (d) VB spectra. The vertical blue lines show the center of the core level. Spectra were taken at a photon energy of 700 eV. (e) V $L_{3,2}$ edge NEXAFS for $Bi_4V_2O_{11}$, collected by the total electron yield. (f) VB spectra for $Bi_4V_2O_{11}$ were collected using incident photon energies of 512.6 eV (off-res), 516.6 eV (e-res), and 518.6 eV (t_2-res).

orbitals. In $BiVO_4$, the gap states were considered extra occupations by electron-doping (such as Mo-doping[14]) and the theoretical calculations revealed that the V 3d character was the predominant component of these gap states.[36] In undoped $Bi_4V_2O_{11}$, the gap states could be attributed to changes in the environment surrounding the V atoms.

As the V coordinates are diversified in orthorhombic $Bi_4V_2O_{11}$, defining the projected orbitals related to crystal field splitting[37] is not straightforward. Nonetheless, linearly polarized X-ray was used to probe the in-plane states (which interact with parallel polarized light ($E_\parallel$)) and out-of-plane states (which interact with perpendicular polarized light ($E_\perp$)) of V 3d characters (Figure 4a). The polarization-dependent V $L_{3,2}$ edge and O K edges NEXAFS spectra are shown in Figure 4b. The NEXAFS spectra collected at two polarizations are similar, implying isotropic orbital coordinates. However, the different spectra reveal details. At the energies where the intensive absorptions (e and t_2) occur in the V L_3 edge, the absorbance intensity difference ($I_\parallel - I_\perp$) under different polarizations is distinctly greater than 0. This suggests that anisotropic unoccupied V 3d states (more unoccupied in-plane states) exist.

In addition, polarized XPS spectra are shown in Figure 4c, measured using the photon energy at the e-resonant absorption according to the NEXAFS results. In the photoemission process, the dipole approximation suggests that the photo-emission intensity can be expressed as follows:[38]

$$I^{\parallel,\perp} \propto |\langle \Psi_f | \hat{A}^{\parallel,\perp} \cdot \hat{p} | \Psi_i \rangle|^2 \qquad (1)$$

where $\langle \Psi_f | \hat{A}^{\parallel,\perp} \cdot \hat{p} | \Psi_i \rangle$ is the matrix element that describes the interaction Hamiltonian between the vector potential of the electromagnetic field $\hat{A}^{\parallel,\perp}$ and the momentum operator $\hat{p}$, with respect to the initial (Ψ_i) and final (Ψ_f) states. When the

initial and final states of electron wavefunction are isotropic, the photoemission intensity ratio is $I^\parallel/I^\perp = (\cos 25° + \sin 25°)^2 \approx 1.77$, as determined from the measurement geometry shown in Figure 4a. If there are no in-plane states, the ratio should be $(\sin 25°)^2 \approx 0.18$. Figure 4c displays the VB spectra at two polarizations with the intensity ratio. The photo-emission intensity of the VB exhibits slight differences in polarizations. Notably, the intensity ratio at the energy of gap states is around 0.99, which is lower than the value in the isotropic condition. This suggests that more out-of-plane states contribute to the gap states, consistent with the presence of more unoccupied in-plane states in the CB. Thus, the gap states are considered the extra occupations of V 3d orbitals and are anisotropic. The analogous gap states in $BiVO_4$ are related to the extra charge in the lattice,[15] and similar anisotropic occupations have been reported in the famous metal–insulator transition of vanadium dioxide.[34,39] Therefore, this anisotropic occupation plays a significant role in the electronic structure of the vanadium oxygen compound.

To further understand the origin of the gap states, the DOS of oxygen-deficient orthorhombic $Bi_4V_2O_{11}$ was simulated. Figure 5a shows that the band gap value of oxygen-deficient $Bi_4V_2O_{11}$ decreases to 1.95 eV. A notable change occurs in the VB edge, where the contribution of Bi 6 s orbitals decreases. This change in the VB is consistent with the observed change in the VB photoemission spectra (Figure S8). After annealing of the film, the states near the VBM increase due to the contribution of Bi 6s orbitals. Another important observation is that gap states appear in oxygen-deficient $Bi_4V_2O_{11}$, comprising both occupied and unoccupied states. The occupied states are located at around 0.71 eV above the VBM and are predominantly composed of V 3d orbitals, consistent with our experimental observations. Figure 5b displays the
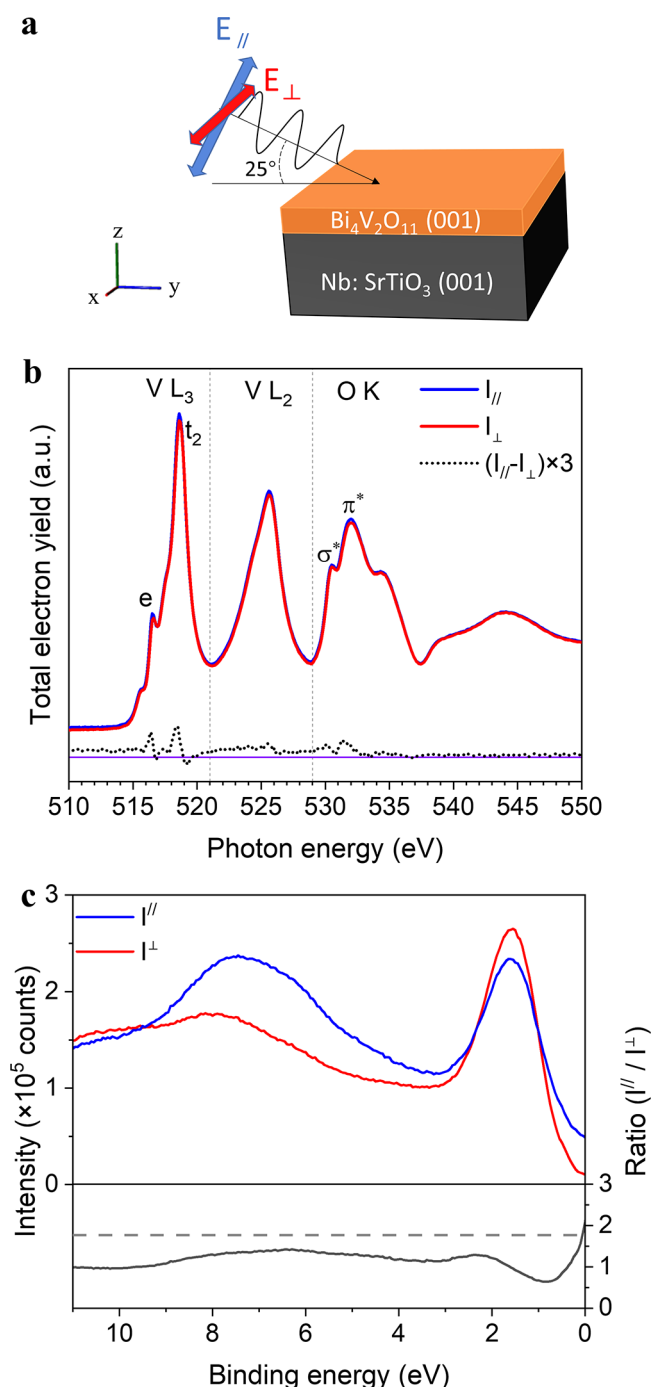
Figure 4. (a) Schematic of the NEXAFS measurement geometry. The X-ray beam is incident at 25° to the sample surface, and the photon polarization is either parallel ($E_{\parallel}$) or perpendicular ($E_{\perp}$) to mirror plane yz. (b) Polarization-dependent V $L_{3,2}$ edge and O K edge NEXAFS spectra are shown in the total electron yield corresponding to $E_{\parallel}$ and $E_{\perp}$. The differences between the two polarizations are also shown concerning the zero-reference line. The vertical dashed lines indicate the approximate energy range from different transitions. (c) VB spectra were measured at a photon energy of 516.6 eV, with two polarizations. The intensity ratio ($I^{\parallel}/I^{\perp}$) is also shown with the reference line located at 1.77.

integrated local densities of states (ILDOS), indicating charge localization in oxygen-deficient $Bi_4V_2O_{11}$. The localization of electrons left after removing a neutral O atom leads to the formation of electronic polarons near the V atom.[40]

Furthermore, the anisotropic localization of electrons around the V surrounding is evident in Figure 5b. It can be inferred that the anisotropic localization of electrons around the V−O tetrahedra results in the emergence of gap states.

The presence of gap states has a significant impact on the electronic structure of materials. To understand the role of gap states in the water oxidation reaction, we conducted a water adsorption experiment to examine the surface potential. The $Bi_4V_2O_{11}$ sample was exposed to a pure H_2O atmosphere (5×10^{-6} Torr) at room temperature to adsorb the water molecules on its surface. The adsorption of H_2O enhanced the gap states, resulting in a shift in ionization potential from 6.32 to 5.92 eV (Figure 6). This suggests that the adsorption of water molecules alters the environment of V atoms, and the surface hydroxyl groups[42] induce extra occupation in V 3d orbitals, leading to gap states as discussed earlier. The adsorbing layer can be removed by annealing the sample at 450 °C (not shown). Additionally, the BE scale can be converted to a scale where the vacuum level is at zero in energy according to the following equation:

$$E_{\text{vac}} = -(E_{\text{VBM}} + \text{IP}) \qquad (2)$$

where E_{vac} is the energy relative to the vacuum level that corresponds to the energy of an electron at rest just outside the solid[43] (Note that it may differ for varied facets of the solid), and E_{VBM} is the difference between BE and the BE at VBM. Ionization potential IP can be determined by measuring the secondary electron cutoff (Figure S10). The comparison between the surface before and after the water adsorption is shown in Figure 6. For the clean surface of $Bi_4V_2O_{11}$, the VBM is almost lower than the water oxidation potential. The existence of gap states results in the occupied states (−5.46 eV) at an energy higher than the water oxidation potential (−5.67 eV). Therefore, the holes there cannot oxidize water thermodynamically. In this study, the water coverage was smaller than that in the actual photocatalysis conditions, i.e., in the solution. Thus, a more significant reduction in IP is expected to make the gap states more unfavorable. The presence of gap states can be understood as an upward shift of VB when considering their role in photocatalytic properties. A significant external potential is necessary to bend the band at the semiconductor‖solution interface and supply the driving potential when the spontaneous oxygen evolution reaction cannot occur. The onset potential in the linear sweep voltammetry curves of epitaxial $Bi_4V_2O_{11}$ is up to 1.1 V vs the reversible hydrogen electrode,[9] reflecting the drawback in the photocatalytic process. This may be why $Bi_4V_2O_{11}$ exhibits unsatisfied performance in water oxidation.[8] Interestingly, $BiVO_4$ is not affected by analogous gap states due to the large ionization potential.[14] Consequently, $Bi_4V_2O_{11}$ exhibits lower photocurrent in the water oxidation reaction than $BiVO_4$ (Figure S11). Based on these results, it may be challenging to eliminate the gap states when using $Bi_4V_2O_{11}$ in a solution. However, using a protection layer on the $Bi_4V_2O_{11}$ surface could effectively eliminate the influence of the local V environment by water molecules. Additionally, strain control of the $Bi_4V_2O_{11}$ films should be one of the potential methods to modify the gap states due to their anisotropic properties.

◼ CONCLUSIONS

In this study, we conducted a comprehensive analysis of the electronic structure of orthorhombic $Bi_4V_2O_{11}$ using a combination of experimental and theoretical strategies. The
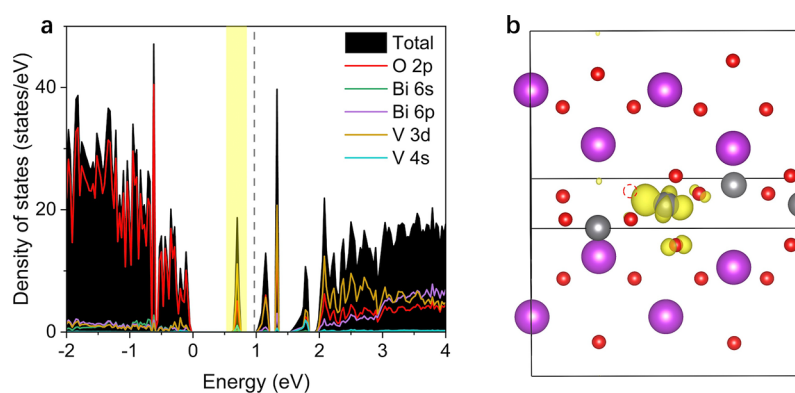
Figure 5. (a) DOS and pDOS plots of orthorhombic $Bi_4V_2O_{11}$ with an oxygen vacancy. The VBM is aligned with zero energy. The dashed line is located at the Fermi level. The gold shadow represents the region from which (b) integrated local densities of states are obtained. The smooth yellow shading shows the isosurface. A dashed circle marks the oxygen vacancy. As for atoms, purple, gray, and red represent Bi, V, and O atoms, respectively.
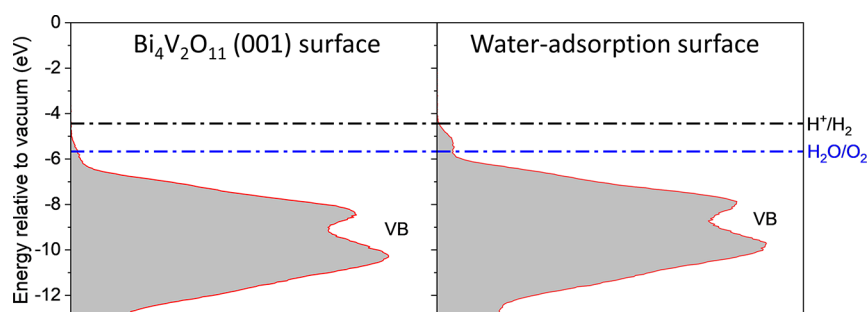
Figure 6. VB photoemission spectra of raw $Bi_4V_2O_{11}$ (001) and water-adsorption surface relative to the vacuum level. The H_2O/O_2 oxidation and the H^+/H_2 reduction standard potentials (T = 298.15 K, pH = 0) are compared.[41]

NEXAFS results confirmed the tetrahedral V local structure in orthorhombic $Bi_4V_2O_{11}$, and DFT calculations utilizing a two-fold superlattice revealed its indirect-band-gap nature and the composition of VB and CB. ARPES was used to experimentally explore the band structure, and the dispersion of top VB was observed, which agreed with the calculated band structure. Additionally, we found gap states in pristine $Bi_4V_2O_{11}$ and investigated them through resonant XPS, polarized XPS, and polarized NEXAFS. We concluded that the gap states originate from the anisotropic localization of electrons around the V−O tetrahedra, and factors such as oxygen vacancies can induce their formation. Water adsorption also caused the enhancement of gap states and induced the unfavorable energy level for water oxidation in $Bi_4V_2O_{11}$, highlighting the importance of controlling them in surface catalysis. Our study suggests that the localization of 3d orbitals plays a significant role in manipulating the electronic structure of analogous oxide materials.

■ ASSOCIATED CONTENT

ⓈI Supporting Information

The Supporting Information is available free of charge at https://pubs.acs.org/doi/10.1021/acs.jpcc.3c01238.

Details of the experimental methods; LEED patterns; experimental and calculated ARPES; XPS spectra; and photoelectrochemical LSV curve (PDF)

■ AUTHOR INFORMATION

Corresponding Author

Takeaki Sakurai − *Faculty of Pure and Applied Sciences, University of Tsukuba, Tsukuba, Ibaraki 305-8573, Japan;* ⓞ orcid.org/0000-0001-5730-1937; Email: sakurai.takeaki.ft@u.tsukuba.ac.jp

Authors

Jiaqi Liu − *Faculty of Pure and Applied Sciences, University of Tsukuba, Tsukuba, Ibaraki 305-8573, Japan;* ⓞ orcid.org/0000-0002-5738-4741

Kenichi Ozawa − *Institute of Materials Structure Science, High Energy Accelerator Research Organization (KEK), Tsukuba, Ibaraki 305-0801, Japan; SOKENDAI (The Graduate University for Advanced Studies), Tsukuba, Ibaraki 305-0801, Japan;* ⓞ orcid.org/0000-0003-2157-4671

Namiki Uezono − *Faculty of Pure and Applied Sciences, University of Tsukuba, Tsukuba, Ibaraki 305-8573, Japan;* ⓞ orcid.org/0000-0001-6894-0515

Sachin A. Pawar − *Faculty of Pure and Applied Sciences, University of Tsukuba, Tsukuba, Ibaraki 305-8573, Japan;* ⓞ orcid.org/0000-0003-0275-1118

Shugo Suzuki − *Faculty of Pure and Applied Sciences, University of Tsukuba, Tsukuba, Ibaraki 305-8573, Japan*

Aboulaye Traoré − *Faculty of Pure and Applied Sciences, University of Tsukuba, Tsukuba, Ibaraki 305-8573, Japan*

Muhammad Monirul Islam − *Faculty of Pure and Applied Sciences, University of Tsukuba, Tsukuba, Ibaraki 305-8573, Japan;* ⓞ orcid.org/0000-0002-9448-731X

Kazuhiko Mase − *Institute of Materials Structure Science, High Energy Accelerator Research Organization (KEK), Tsukuba, Ibaraki 305-0801, Japan; SOKENDAI (The Graduate University for Advanced Studies), Tsukuba, Ibaraki 305-0801, Japan*

Complete contact information is available at:
https://pubs.acs.org/10.1021/acs.jpcc.3c01238

Author Contributions

The manuscript was written through contributions of all authors. All authors have given approval to the final version of the manuscript.

Notes

The authors declare no competing financial interest.

■ REFERENCES

(1) Lv, P.; Zheng, M.; Wang, X.; Huang, F. Subsolidus Phase Relationships and Photocatalytic Properties in the Ternary System TiO_2–Bi_2O_3–V_2O_5. *J. Alloys Compd.* **2014**, *583*, 285−290.

(2) Lu, Y.; Pu, Y.; Wang, J.; Qin, C.; Chen, C.; Seo, H. J. On Structure and Methylene Blue Degradation Activity of an Aurivillius-Type Photocatalyst of $Bi_4V_2O_{11}$ Nanoparticles. *Appl. Surf. Sci.* **2015**, *347*, 719−726.

(3) Lee, D.; Wang, W.; Zhou, C.; Tong, X.; Liu, M.; Galli, G.; Choi, K.-S. The Impact of Surface Composition on the Interfacial Energetics and Photoelectrochemical Properties of $BiVO_4$. *Nat. Energy* **2021**, *6*, 287−294.

(4) Lin, Y.; Cai, H.; Chen, H.; Luo, H. One−Pot Synthesis of $Bi_4V_2O_{11}$/$BiVO_4$ Heterostructure with Enhanced Photocatalytic Activity for Dye Degradation. *Appl. Surf. Sci.* **2021**, *544*, No. 148921.

(5) Zhao, Y.; Liu, X.; Gu, S.; Liu, J. Enhanced Photocatalytic Performance of Rhodamine B and Enrofloxacin by Pt Loaded $Bi_4V_2O_{11}$: Boosted Separation of Charge Carriers, Additional Superoxide Radical Production, and the Photocatalytic Mechanism. *RSC Adv.* **2021**, *11*, 9746−9755.

(6) Mairesse, G.; Roussel, P.; Vannier, R. N.; Anne, M.; Pirovano, C.; Nowogrocki, G. Crystal Structure Determination of α, β and γ-$Bi_4V_2O_{11}$ Polymorphs. Part I: γ and β- $Bi_4V_2O_{11}$. *Solid State Sci.* **2003**, *5*, 851−859.

(7) Mairesse, G.; Roussel, P.; Vannier, R. N.; Anne, M.; Nowogrocki, G. Crystal Structure Determination of α-, β- and γ-$Bi_4V_2O_{11}$ Polymorphs. Part II: Crystal Structure of α-$Bi_4V_2O_{11}$. *Solid State Sci.* **2003**, *5*, 861−869.

(8) Jiang, Z.; Liu, Y.; Li, M.; Jing, T.; Huang, B.; Zhang, X.; Qin, X.; Dai, Y. One-Pot Solvothermal Synthesis of $Bi_4V_2O_{11}$ as A New Solar Water Oxidation Photocatalyst. *Sci. Rep.* **2016**, *6*, 22727.

(9) Song, J.; Choi, K. S.; Seo, M. J.; Jo, Y.-R.; Lee, J.; Kim, T. L.; Jeong, S. Y.; An, H.; Jang, H. W.; Kim, B.-J.; Jeon, C.; Lee, S. Nonequilibrium Deposition in Epitaxial $BiVO_4$ Thin Film Photoanodes for Improving Solar Water Oxidation Performance. *Chem. Mater.* **2018**, *30*, 5673−5681.

(10) Lv, C.; Chen, G.; Zhou, X.; Zhang, C.; Wang, Z.; Zhao, B.; Li, D. Oxygen-Induced Bi^{5+}-Self-Doped $Bi_4V_2O_{11}$ with a p−n Homojunction Toward Promoting the Photocatalytic Performance. *ACS Appl. Mater. Interfaces* **2017**, *9*, 23748−23755.

(11) Yue, Y.; Dzięgielewska, A.; Krok, F.; Whiteley, R. M.; Toms, H.; Malys, M.; Yan, H.; Abrahams, I. Local Structure and Conductivity in the BIGAVOX System. *J. Phys. Chem. C* **2022**, *126*, 2108−2120.

(12) Touboul, M.; Lokaj, J.; Tessier, L.; Kettman, V.; Vrabel, V. Structure of Dibismuth Vanadate $Bi_2VO_{5.5}$. *Acta Crystallogr. C* **1992**, *48*, 1176−1179.

(13) Mohamed, M.; May, M. M.; Kanis, M.; Brützam, M.; Uecker, R.; van de Krol, R.; Janowitz, C.; Mulazzi, M. The Electronic Structure and the Formation of Polarons in Mo-Doped $BiVO_4$ Measured by Angle-Resolved Photoemission Spectroscopy. *RSC Adv.* **2019**, *9*, 15606−15614.

(14) Favaro, M.; Uecker, R.; Nappini, S.; Píš, I.; Magnano, E.; Bluhm, H.; van de Krol, R.; Starr, D. E. Chemical, Structural, and Electronic Characterization of the (010) Surface of Single Crystalline Bismuth Vanadate. *J. Phys. Chem. C* **2019**, *123*, 8347−8359.

(15) Chaudhuri, A.; Mandal, L.; Chi, X.; Yang, M.; Scott, M. C.; Motapothula, M.; Yu, X. J.; Yang, P.; Shao-Horn, Y.; Venkatesan, T.; Wee, A. T. S.; Rusydi, A. Direct Observation of Anisotropic Small-Hole Polarons in an Orthorhombic Structure of $BiVO_4$ Films. *Phys. Rev. B* **2018**, *97*, No. 195150.

(16) Giannozzi, P.; Baroni, S.; Bonini, N.; Calandra, M.; Car, R.; Cavazzoni, C.; Ceresoli, D.; Chiarotti, G. L.; Cococcioni, M.; Dabo, I.; et al. QUANTUM ESPRESSO: A Modular and Open-Source Software Project for Quantum Simulations of Materials. *J. Phys.: Condens. Matter* **2009**, *21*, No. 395502.

(17) Giannozzi, P.; Andreussi, O.; Brumme, T.; Bunau, O.; Buongiorno Nardelli, M.; Calandra, M.; Car, R.; Cavazzoni, C.; Ceresoli, D.; Cococcioni, M.; et al. Advanced Capabilities for Materials Modelling with Quantum ESPRESSO. *J. Phys.: Condens. Matter* **2017**, *29*, 465901.

(18) Giannozzi, P.; Baseggio, O.; Bonfà, P.; Brunato, D.; Car, R.; Carnimeo, I.; Cavazzoni, C.; de Gironcoli, S.; Delugas, P.; Ferrari Ruffino, F.; Ferretti, A.; Marzari, N.; Timrov, I.; Urru, A.; Baroni, S. Quantum ESPRESSO toward the Exascale. *J. Chem. Phys.* **2020**, *152*, 154105.

(19) Prandini, G.; Marrazzo, A.; Castelli, I. E.; Mounet, N.; Marzari, N. Precision and Efficiency in Solid-State Pseudopotential Calculations. *npj Comput. Mater.* **2018**, *4*, 72.

(20) Momma, K.; Izumi, F. VESTA3 for Three-Dimensional Visualization of Crystal, Volumetric and Morphology Data. *J. Appl. Crystallogr.* **2011**, *44*, 1272−1276.

(21) Masui, S.; Shigemasa, E.; Yagishita, A. Upgrade and Recent Performance of 24-m SGM at the Photon Factory. *Rev. Sci. Instrum.* **1992**, *63*, 1330−1333.

(22) Toyoshima, A.; Kikuchi, T.; Tanaka, H.; Mase, K.; Amemiya, K. In Situ Removal of Carbon Contamination from a Chromium-Coated Mirror: Ideal Optics to Suppress Higher-Order Harmonics in the Carbon K -Edge Region. *J. Synchrotron Radiat.* **2015**, *22*, 1359−1363.

(23) Ozawa, K.; Aiura, Y.; Wakabayashi, D.; Tanaka, H.; Kikuchi, T.; Toyoshima, A.; Mase, K. Beamline Commissioning for Microscopic Measurements with Ultraviolet and Soft X-Ray Beam at the Upgraded Beamline BL-13B of the Photon Factory. *J. Synchrotron Radiat.* **2022**, *29*, 400−408.

(24) Toyoshima, A.; Kikuchi, T.; Tanaka, H.; Mase, K.; Amemiya, K.; Ozawa, K. Performance of PF BL-13A, a Vacuum Ultraviolet and Soft X-Ray Undulator Beamline for Studying Organic Thin Films Adsorbed on Surfaces. *J. Phys. Conf. Ser.* **2013**, *425*, No. 152019.

(25) Seah, M. P.; Smith, G. C.; Anthony, M. T. AES: Energy Calibration of Electron Spectrometers. I-an Absolute, Traceable Energy Calibration and the Provision of Atomic Reference Line Energies. *Surf. Interface Anal.* **1990**, *15*, 293−308.

(26) de Groot, F. M. F. X-Ray Absorption and Dichroism of Transition Metals and Their Compounds. *J. Electron Spectrosc. Relat. Phenomena* **1994**, *67*, 529−622.

(27) Setyawan, W.; Curtarolo, S. High-Throughput Electronic Band Structure Calculations: Challenges and Tools. *Comput. Mater. Sci.* **2010**, *49*, 299−312.

(28) Cooper, J. K.; Gul, S.; Toma, F. M.; Chen, L.; Glans, P. A.; Guo, J.; Ager, J. W.; Yano, J.; Sharp, I. D. Electronic Structure of Monoclinic BiVO$_4$. *Chem. Mater.* **2014**, *26*, 5365−5373.

(29) Zhao, Z.; Li, Z.; Zou, Z. Electronic Structure and Optical Properties of Monoclinic Clinobisvanite BiVO$_4$. *Phys. Chem. Chem. Phys.* **2011**, *13*, 4746.

(30) Lv, B.; Qian, T.; Ding, H. Angle-Resolved Photoemission Spectroscopy and Its Application to Topological Materials. *Nat. Rev. Phys.* **2019**, *1*, 609−626.

(31) Payne, D. J.; Robinson, M. D. M.; Egdell, R. G.; Walsh, A.; McNulty, J.; Smith, K. E.; Piper, L. F. J. The Nature of Electron Lone Pairs in BiVO$_4$. *Appl. Phys. Lett.* **2011**, *98*, 212110.

(32) Pastor, E.; Park, J.-S.; Steier, L.; Kim, S.; Grätzel, M.; Durrant, J. R.; Walsh, A.; Bakulin, A. A. In Situ Observation of Picosecond Polaron Self-Localisation in α-Fe$_2$O$_3$ Photoelectrochemical Cells. *Nat. Commun.* **2019**, *10*, 3962.

(33) Starr, D. E.; Favaro, M.; Abdi, F. F.; Bluhm, H.; Crumlin, E. J.; van de Krol, R. Combined Soft and Hard X-Ray Ambient Pressure Photoelectron Spectroscopy Studies of Semiconductor/Electrolyte Interfaces. *J. Electron Spectrosc. Relat. Phenomena* **2017**, *221*, 106−115.

(34) Aetukuri, N. B.; Gray, A. X.; Drouard, M.; Cossale, M.; Gao, L.; Reid, A. H.; Kukreja, R.; Ohldag, H.; Jenkins, C. A.; Arenholz, E.; et al. Control of the Metal−Insulator Transition in Vanadium Dioxide by Modifying Orbital Occupancy. *Nat. Phys.* **2013**, *9*, 661−666.

(35) Jovic, V.; Laverock, J.; Rettie, A. J. E.; Zhou, J.-S.; Mullins, C. B.; Singh, V. R.; Lamoureux, B.; Wilson, D.; Su, T.-Y.; Jovic, B.; et al. Soft X-Ray Spectroscopic Studies of the Electronic Structure of M:BiVO$_4$ (M = Mo, W) Single Crystals. *J. Mater. Chem. A* **2015**, *3*, 23743−23753.

(36) Kweon, K. E.; Hwang, G. S.; Kim, J.; Kim, S.; Kim, S. Electron Small Polarons and Their Transport in Bismuth Vanadate: A First Principles Study. *Phys. Chem. Chem. Phys.* **2015**, *17*, 256−260.

(37) Cao, Y.; Liu, X.; Shafer, P.; Middey, S.; Meyers, D.; Kareev, M.; Zhong, Z.; Kim, J.-W.; Ryan, P. J.; Arenholz, E.; Chakhalian, J. Anomalous Orbital Structure in a Spinel−Perovskite Interface. *npj Quant. Mater.* **2016**, *1*, 16009.

(38) Yukawa, R.; Yamamoto, S.; Ozawa, K.; D'Angelo, M.; Ogawa, M.; Silly, M. G.; Sirotti, F.; Matsuda, I. Electronic Structure of the Hydrogen-Adsorbed SrTiO$_3$ (001) Surface Studied by Polarization-Dependent Photoemission Spectroscopy. *Phys. Rev. B* **2013**, *87*, No. 115314.

(39) Haverkort, M. W.; Hu, Z.; Tanaka, A.; Reichelt, W.; Streltsov, S. V.; Korotin, M. A.; Anisimov, V. I.; Hsieh, H. H.; Lin, H.-J.; Chen, C. T.; et al. Orbital-Assisted Metal-Insulator Transition in VO$_2$. *Phys. Rev. Lett.* **2005**, *95*, No. 196404.

(40) Cheng, C.; Fang, Q.; Fernandez-Alberti, S.; Long, R. Controlling Charge Carrier Trapping and Recombination in BiVO$_4$ with the Oxygen Vacancy Oxidation State. *J. Phys. Chem. Lett.* **2021**, *12*, 3514−3521.

(41) Trasatti, S. The Absolute Electrode Potential: An Explanatory Note (Recommendations 1986). *Pure Appl. Chem.* **1986**, *58*, 955−966.

(42) Benkoula, S.; Sublemontier, O.; Patanen, M.; Nicolas, C.; Sirotti, F.; Naitabdi, A.; Gaie-Levrel, F.; Antonsson, E.; Aureau, D.; Ouf, F.-X.; et al. Water Adsorption on TiO$_2$ Surfaces Probed by Soft X-Ray Spectroscopies: Bulk Materials vs. Isolated Nanoparticles. *Sci. Rep.* **2015**, *5*, 15088.

(43) Ishii, H.; Sugiyama, K.; Ito, E.; Seki, K. Energy Level Alignment and Interfacial Electronic Structures at Organic/Metal and Organic/Organic Interfaces. *Adv. Mater.* **1999**, *11*, 605−625.